Microstructural and mechanical characterisation of a second generation hybrid metal extrusion & bonding aluminium-steel butt joint

Tina Bergh [a],[*], Lise Sandnes [b], Duncan Neil Johnstone [c], Øystein Grong [b], Filippo Berto [b], Randi Holmestad [a], Paul Anthony Midgley [c], Per Erik Vullum [a]

[a] Department of Physics, Norwegian University of Science and Technology (NTNU), Høgskoleringen 5, 7491 Trondheim, Norway
[b] Department of Mechanical and Industrial Engineering, NTNU, Richard Birkelands vei 2b, 7491 Trondheim, Norway
[c] Department of Materials Science and Metallurgy, University of Cambridge, 27 Charles Babbage Road, Cambridge, CB3 0FS, UK

ARTICLE INFO

ABSTRACT

Hybrid metal extrusion & bonding (HYB) is a joining method that enables solid-state bonding by combining addition of aluminium filler material through continuous extrusion with pressure exerted by a rotating steel tool. This work presents mechanical and microstructural characterisation of a second generation HYB butt joint of aluminium alloy 6082 and structural steel S355. The ultimate tensile strength was measured to be in the range of 184–220 MPa, which corresponds to 60–72% joint efficiency. Digital image correlation analysis of the strain development during tensile testing revealed that root cracks formed, before the final fracture ran close to the aluminium-steel interface. A significant amount of residual aluminium was found on the steel fracture surface, especially in regions that experienced higher pressure during joining. Scanning and transmission electron microscopy revealed that the bond strength could be attributed to a combination of microscale mechanical interlocking and a discontinuous nanoscale interfacial Al-Fe-Si intermetallic phase layer. Analysis of scanning electron diffraction data acquired in a tilt series, indicated that the polycrystalline intermetallic phase layer contained the cubic α_c phase. The results give insight into the bonding mechanisms of aluminium-steel joints and into the performance of HYB joints, which may be used to better understand and further develop aluminium-steel joining processes.

1. Introduction

Joints between aluminium (Al) alloys and steels have a wide range of applications, especially in the automotive industry, due to the favourable combination of the high strength of steels and the low weight of Al alloys. However, obtaining sound Al-steel joints is challenging by traditional welding processes, due to the large differences in thermophysical properties. In addition, heat applied or generated during joining may lead to a soft zone on the Al side of the joint, and the formation of brittle interfacial Al-Fe(-Si) intermetallic phases (IMPs) along the bonded interface, that can limit the mechanical properties of the joint [1–4]. Despite these challenges, several joining processes have been adopted to produce sound Al-steel joints [5], e.g. friction stir welding (FSW) [6] and laser welding-brazing [7]. Various innovative hybrid joining techniques that combine valuable aspects of other existing techniques have evolved, including e.g. laser-assisted FSW [8] and the recently developed hybrid metal extrusion & bonding (HYB) process

[9].

HYB is a solid state joining method originally developed for butt joining of Al alloy plates [9–11] that has developed into a versatile method for joining of a range of metallic alloys in various configurations [12–14]. The basis of the HYB method is continuous extrusion of a filler material (FM) that is dragged by a rotating steel tool through a non-rotating extruder housing and subsequently squeezed into the weld groove. The addition of FM and the pressure exerted by the rotating tool enable joining at low temperature, which is an advantage for Al-steel joining. By considering the low process temperature and utilising an analytical framework for modelling of Al-Fe interdiffusion, it was found that an IMP layer on the nanoscale was expected for HYB Al-steel joints, which was supported by transmission electron microscopy (TEM) [15]. The first generation of HYB Al-steel joints produced had ultimate tensile strength (UTS) values in the range of 104–140 MPa [16]. These joints suffered from a lack of bonding along a significant portion of the bond line. Still, the HYB process holds great potential for Al-steel joining, and

* Corresponding author.
  E-mail address: tina.bergh@ntnu.no (T. Bergh).

more research is needed to optimise the process, explain the underlying bonding mechanisms, and characterise the observed nanoscale IMP layer.

This work presents characterisation of a second generation HYB Al-steel butt joint, produced following improvements of the setup used for the first generation HYB Al-steel joints. By combining mechanical and microstructural characterisation, this study aims to contribute to better understanding of the performance of Al-steel HYB joints and of the underlying bonding mechanisms. This work also provides fundamental insight into solid state Al-steel bonding in general.

2. Materials and methods

2.1. Materials

The FM was a wire of Al alloy 6082 (Ø 1.2 mm), that was manufactured starting with homogenised direct chill cast billets that were hot extruded, quenched and naturally aged, before they were cold drawn and cold shaved. The base materials (BMs) were a plate of rolled Al alloy 6082-T6 and a rolled structural steel S355 (EN 10025–2) plate, both with the following dimensions; length 240 mm, width 120 mm and thickness 4 mm. The nominal alloy compositions are given in Tables 1 and 2. Prior to joining, the edge of the steel plate was machined to obtain a bevelled edge that fitted the shape of the rotating pin. The Al and steel plates were subsequently cleaned with acetone.

2.2. Hybrid metal extrusion & bonding

Schematic illustrations of the HYB process are shown in Fig. 1. Prior to joining, the BMs were placed on top of a steel backing and fastened so that a 2 mm root opening formed between them, as shown in Fig. 1(a). A HYB PinPoint extruder tool [17] was positioned so that it did not touch the steel plate but was in direct contact with the edge of the Al BM plate. The extruder tool consisted of a steel housing that surrounded a rotating pin equipped with a set of extrusion dies in the bottom end. The steel BM was placed on the advancing side (AS), where the pin rotation was in the same direction as its movement along the weld groove, and oppositely, the Al BM was placed on the retreating side (RS), following the nomenclature used in FSW [18]. During HYB, the extruder travelled along the groove, as illustrated in Fig. 1(b), and heavily deformed the edge of the Al BM by digging into and dragging the Al BM around. Simultaneously, the Al FM wire was continuously fed into the extruder where it was dragged around due to the frictional forces acting on it inside the extrusion chamber, i.e. the space in between the rotating pin and the non-rotating steel housing. After meeting an abutment inside the extrusion chamber, the FM was extruded through moving helicoid-shaped dies at the bottom end of the rotating pin. The Al FM was dragged along with the pin before it became deposited in the groove behind the pin. The flow of Al in the groove resulted in bonding and eventually a consolidated joint, as illustrated in Fig. 1(c). Further descriptions of the HYB process can be found elsewhere [11,19,20].

The joining parameters used were; pin rotation: 400 RPM, welding speed: 6 mm/s and wire feed rate: 142 mm/s. During joining, the FM inlet in the extruder was cooled by spraying with dry ice supplied at a rate of 160 g/min. The gross heat input during welding was estimated to ~0.27 kJ/mm.

2.3. Hardness measurements

The Vickers hardness of polished cross-sections of the FM wire was measured before joining using an Innovatest Nova 360 instrument and an applied load of 0.5 kg. The hardnesses of the Al and steel BMs were measured before joining on polished specimens using a Mitutoyo micro Vickers hardness testing machine and an applied load of 1.0 kg. The transverse hardness profiles of polished cross-sections of the joint were measured following the same procedure as for the BMs.

2.4. Tensile testing

For tensile testing of the joint, four specimens were prepared with dimensions according to ASTM standard E8/E8M [21], except that the parallel lengths were extended to 36 mm to capture the entire soft zone on the Al side. Two of the specimens, R1 and R2, were tested as-joined with the reinforcement intact. Two other specimens, F1 and F2, were flush-machined prior to testing, in order to remove the excess material at the top (crown) and bottom (root) of the joint. Tensile testing was performed using an Instron 5985 hydraulic test machine equipped with a load cell of 250 kN. During all tensile tests the cross-head speed was set to 1.5 mm/min, which corresponds to a nominal strain rate of ~7e-4 s^{-1}.

Two-dimensional DIC analysis were performed to quantify the strain evolution occurring during tensile testing. Before testing, the specimens were each painted with a fine grained speckle pattern that was monitored during tensile testing with a high-resolution camera recording at ~10 Hz. The images were analysed using the software developed by Fagerholt et al. [22,23], that is based on calculating the displacements of finite elements in the speckle pattern by cross-correlation. This was done by first adding a mesh onto a reference image of the speckle pattern on the specimen taken before tensile testing, before projecting the mesh onto each image taken during testing. For each element in the mesh, the translation of the speckle pattern was calculated by cross-correlation with respect to the corresponding mesh element in the reference image. The displacement of the speckle pattern was then used to calculate the in-plane principal true strains that were in turn used to calculate the effective strain. The effective strains were finally visualised as two-dimensional strain-field maps.

2.5. Optical microscopy

The macrostructure of Al was imaged in mechanically polished cross-sections that had been leached in a solution of 100 ml H_2O and 1 g NaOH for 3 − 4 min, using an Alicona infinite focus confocal microscope. In order to reveal the Al microstructure, polished cross-sections were anodised by immersion in a solution containing H_2O and 5% HBF_4 (Barker's reagent [24]) for 90 s using a current of 1.0 A and a voltage of 20 V. A Leica MEF4M optical microscope was used to examine the microstructure in polarised light.

2.6. Scanning electron microscopy

Scanning electron microscopy (SEM) studies were conducted on mechanically polished cross-sections of the joint and on original fracture surfaces resulting from tensile testing. The SEM imaging was performed using a FEI Helios G4 dual-beam focused ion beam (FIB)-SEM instrument at acceleration voltages in the range of 3 − 15 kV.

Table 1
Nominal compositions of the 6082 Al alloys used as FM and BM in wt%.

	Si	Mg	Mn	Fe	Cr	Cu	Ti	Zr	Zn	B	Other
Al FM	1.11	0.61	0.51	0.2	0.14	0.002	0.043	0.13	–	0.006	0.029
Al BM	0.9	0.8	0.42	0.45	0.02	0.06	0.02	–	0.05	–	0.02

Table 2
Nominal composition of the structural steel S355 BM in wt%.

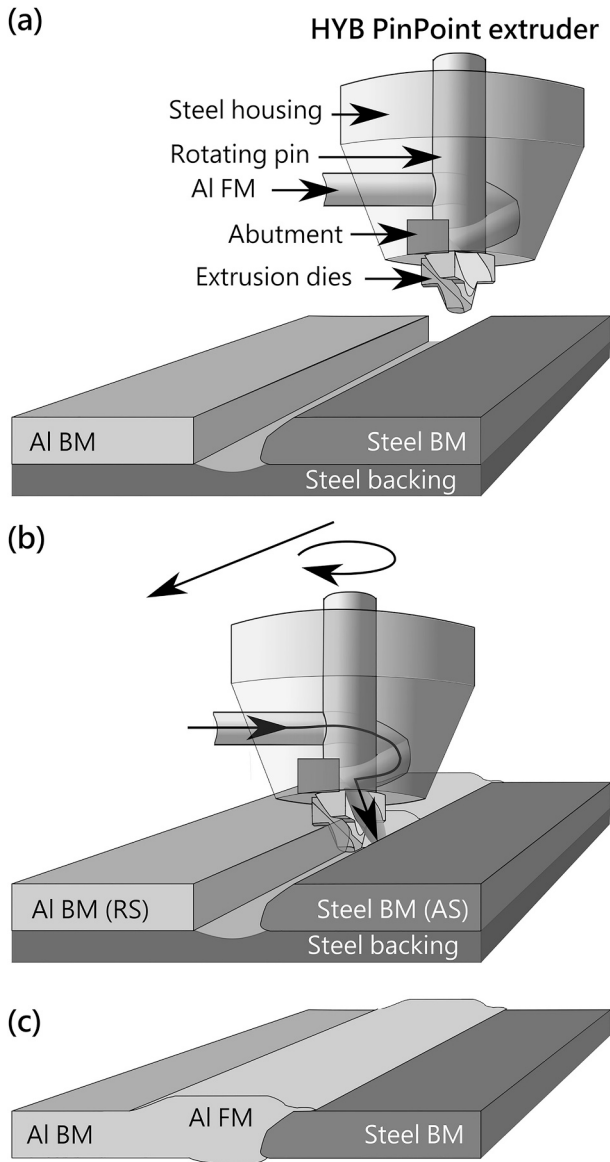| Mn	C	Cr	Ni	Al	Cu	Si	Nb	P	Mo	V	S	N	Ti	B
0.69	0.067	0.05	0.05	0.040	0.028	0.02	0.014	0.010	0.009	0.008	0.005	0.005	0.001	0.0001

Fig. 1. Illustration (not to scale) of (a) before, (b) during and (c) after Al-steel HYB butt joining. Before joining, Al and steel BM plates are clamped onto a steel backing, Al on the retreating side (RS) and steel on the advancing side (AS). During joining, the HYB PinPoint extruder travels along the joint line as the Al FM wire is continuously extruded through extrusion dies in the rotating pin, after meeting an abutment inside the extrusion chamber. The Al FM fills the groove, and a finished joint is produced.

2.7. Transmission electron microscopy

TEM lamellae were prepared from joint cross-sections and fracture surfaces by FIB lift-out. TEM lamellae of improved quality were obtained by rotating each cross-section so that the FIB thinning was performed normal to the Al-steel interface, in order to limit thickness variations due to the difference in milling rates between Al and steel.

TEM, scanning TEM (STEM), and X-ray energy dispersive spectroscopy (EDS) were performed using a JEOL ARM200CF fitted with CEOS spherical aberration correctors in both the probe and image forming optics. The microscope was operated at 200 kV and was equipped with a 100 mm^2 Centurio EDS detector. EDS maps were analysed and visualised using the python library hyperspy [25] to bin and fit the data and to estimate the composition using the Cliff-Lorimer method, as described in detail in Supplementary Information (SI) S1.

Scanning electron diffraction (SED) data were acquired using a JEOL ARM300F (Diamond Light Source, UK) fitted with JEOL spherical aberration correctors in both the probe and image forming optics. The instrument was operated at 200 kV and aligned in an uncorrected nanobeam configuration with a convergence semi-angle of <1 mrad and a diffraction limited probe diameter of ~5 nm. Diffraction patterns were acquired using a Merlin Medipix direct electron detector with an exposure time of 1 ms at each probe position. SED maps were obtained from the same specimen region at a series of specimen tilt conditions covering a range of 30° in steps of 1°.

The SED data were analysed using the python library pyxem [26]. Diffraction contrast images of crystals in the mapped area were produced using virtual dark field (VDF) imaging-based segmentation [27]. VDF images were formed by plotting the intensity within integration windows, positioned to capture measured Bragg diffraction disks, as a function of probe position. Individual crystals in each VDF image were isolated by watershed image segmentation. Further, since several diffraction spots were typically detected for each crystal, VDF image segments associated with the same crystal were identified via cross-correlation and summed.

The crystal structure of observed IMPs was assessed based on diffraction patterns recorded near zone-axis orientations that were selected manually from the SED data. Non-negative matrix factorisation based segmentation [27,28] was performed using the SED data from a small region of interest including each IMP particle, in order to reduce diffuse scattering and overlapping crystal contributions. Bragg disk positions were then found and the distances between spots in selected rows were calculated. For each selected row, all measured distances between spots ($|\Delta \vec{G}|$) were used to compute an average d-spacing ($|\Delta \vec{G}|^{-1}$) and standard deviation. Indexation of the Bragg peaks was then attempted with respect to numerous candidate Al-Fe(-Si) phases, as detailed in SI S2. For this, the two shortest average diffraction spot distances for two non-parallel rows and the angle between these, were considered for each pattern. The phase(s) that best matched with as many patterns as possible was identified. More information on the SED data acquisition and analysis can be found in SI S2.

3. Results

3.1. Mechanical characterisation

To investigate the influence of the joining process on the starting materials, Vickers hardness profiles were measured across joint cross-sections and compared to the hardness of the materials as-received. In the as-received condition, the hardness of the steel BM, Al BM and Al FM were measured to 162.7 ± 4.5 HV$_{1.0}$ (average and standard deviation of 21 measurements), 107.2 ± 1.7 HV$_{1.0}$ (14) and 124.5 ± 2.2 HV$_{0.5}$ (15), respectively. Fig. 2(a) presents horizontal and vertical hardness profiles measured across joint cross-sections. Fig. 2(b) shows a corresponding
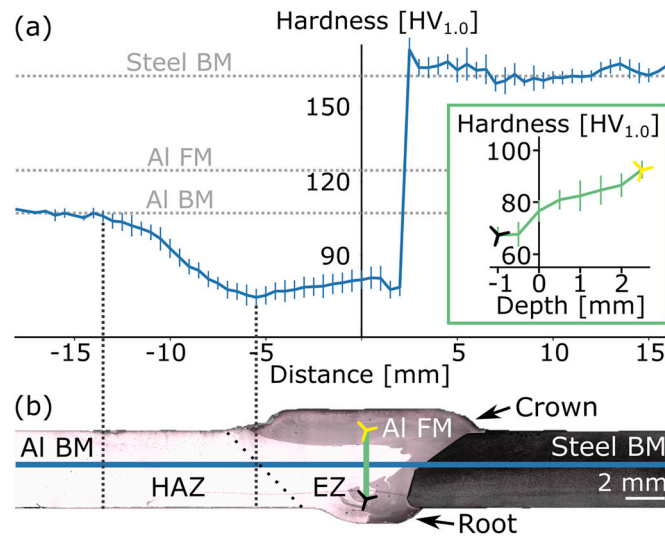
Fig. 2. Hardness profiles of joint cross-sections. (a) Average horizontal and vertical profiles displayed in blue and green, based on six and five measured profiles, respectively. The error bars show plus and minus one standard deviation. The horizontal grey lines show the hardness of the steel BM, Al FM and Al BM before joining. The vertical lines at −13.5 mm and −5.5 mm indicate the extent of the soft zone in Al and the minimum value in the horizontal profile, respectively. (b) Optical micrograph with coloured lines that mark the positions of the hardness indents. The locations of the root and crown regions, the heat affected zone (HAZ) and the extrusion zone (EZ) are indicated. (For interpretation of the references to colour in this figure legend, the reader is referred to the web version of this article.)

optical microscopy image where the location of the hardness profile indents are indicated. By comparing the horizontal profile in Fig. 2(a) with the micrograph in (b), it is apparent that the steel showed no decrease in hardness after joining, while Al showed significant softening both inside and outside of the extrusion zone (EZ). The horizontal profile shows a heat affected zone (HAZ) extending 13.5 mm into the Al BM, and the minimum hardness (73.1 $HV_{1.0}$) was found near the EZ-HAZ boarder, 5.5 mm from the weld centre. The vertical profile shows that the hardness decreased from the weld crown at the top towards the weld root region at the bottom.

The engineering stress-strain curve obtained via tensile testing is shown in Fig. 3(a) for specimen R2, while the curves for the other specimens are shown in SI S3. The average UTS was 197 ± 15 MPa, and the average fracture strain was 2.5 ± 0.7%. Considering that the UTS of the Al BM before joining was 307 MPa and that the fracture strain was ~20% [29], the average joint efficiency was 64 ± 5%, and the fracture

strain was low. Specimen F1 had the highest UTS of 220 MPa (72%) and R1 and R2 the lowest of 184 MPa (60%). Strain hardening can be observed in Fig. 3(a), and the final fracture was brittle with limited necking occurring.

DIC analyses were performed to study the crack initiation and propagation path, as well as the local deformations occurring during tensile testing. Figs. 3(b) and (c) show images and strain maps of specimen R2 at different stages (I-IV) during tensile testing. From (b) it can be seen that a crack developed near the interface between steel and Al in the root region (I). With increasing stress, the root crack propagated (II and III), and also a smaller crack became visible in the weld crown region (III). The final fracture occurred close to the Al-steel interface (IV). Fig. 3(c) shows strain maps displaying the effective strain. First, strain developed in the soft Al zone and in the vicinity of the root crack (I). As the applied load increased, the deformation increased in both of these regions (II), before the strain became significant also along the Al-steel
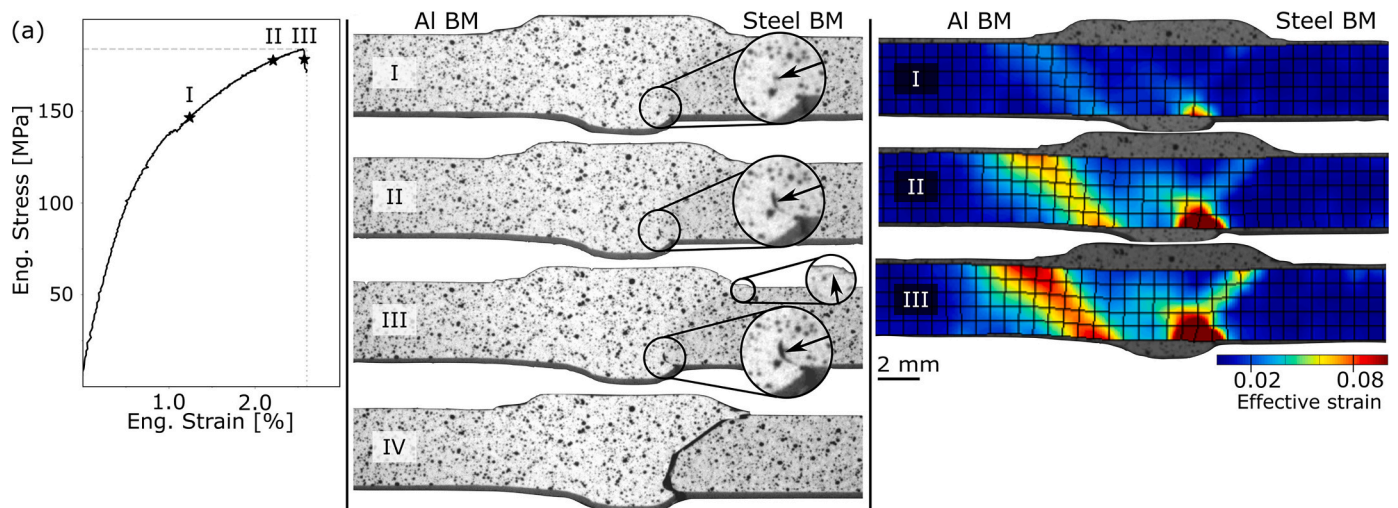

Fig. 3. Tensile testing of specimen R2. (a) Engineering stress-strain curve where selected points (I-III) are marked. (b) Images used for digital image correlation (DIC) analysis at stages I-III and immediately after fracture (IV). The speckle pattern used in the DIC analysis, consisting of black dots painted on top of a light background, can be seen. The insets highlight crack formation. (c) Strain maps, resulting from the DIC analysis, showing the effective strain at stages I-III.

interface (III). Results from the DIC analysis of specimens R1, F1 and F2 are shown in SI S3. For all tested specimens, the fracture propagated from root flaws and subsequently along the Al-steel interface.

To better understand the fracture path, the fracture surfaces from tensile testing were imaged by SEM. Figs. 4(a) and (b) show an optical micrograph together with back-scatter electron (BSE) and secondary electron (SE) SEM images of the steel fracture surface of specimen R2. The surface showed two distinct characteristics; i) a flat appearance in the top towards the crown (left side of the blue lines in Figs. 4(a) and (b)) and ii) a wavy appearance in the bottom part towards the root region (right side). The flat upper part showed residual Al that had stuck to the steel surface forming thin, elongated chunks. The wavy pattern in the lower region consisted of thick chunks of Al attached to the steel with large bumps and protrusions. The corresponding Al fracture surface showed a wavy pattern with bumps and dimples matching those on the steel surface, as shown in SI S4. The shape of this pattern indicated that it resulted from an impression of the extrusion dies in Al as the rotating pin traversed the weld groove. From both the steel and the Al fracture surfaces, it could be seen that the fracture ran mainly along the Al-steel interface for the upper part, although there was a noticeable amount of residual material. The fracture ran mostly in Al for the lower part, except for the bottom of the root, where the fracture ran close to the Al-steel interface.

3.2. Microstructural characterisation

A micrograph of the joint cross-section is shown in Fig. 5(a) (enlarged view of Fig. 2(b)), where the Al BM appears brighter than the Al FM. The contrast difference arose after leaching and stemmed from the differences in chemical compositions, which resulted in a difference in overall leaching behaviour for the BM and FM. The top weld region including the crown and the Al region adjacent to steel were predominantly composed of Al FM, while the Al BM was pushed into the centre of the weld groove and into the root region. Fig. 5(b) displays the grain structure in the Al region imaged in polarised light after anodisation. Most of the grains in the EZ were smaller than those in the HAZ. The middle region of the EZ comprised fine equiaxed grains, while the bottom region showed larger grains reflecting the Al flow pattern. Series of elliptical features, resembling an onion ring pattern, can be seen in the top weld crown. Figs. 5(a) and (b) both indicate that the FM flow was directed downward along the steel side of the weld groove and towards the root region, where the FM met the Al BM.

3.2.1. The aluminium-steel interface region

The Al-steel interface region was studied by SEM, as shown in Fig. 6. An overview of the weld cross-section is shown in Fig. 6(a), where steel fragments of various sizes can be seen in the root region. These steel fragments resulted from the rotating pin coming into contact with the steel surface with enough force to detach steel fragments that were stirred into the EZ. Figs. 6(b), (c) and (d) display higher magnification BSE SEM images of the Al-steel interface showing the rough appearance of the interface, which was more pronounced towards the bottom half of the joint. A steel protrusion with dimensions ~20 μm can be seen in Fig. 6(c). (d) reveals an interfacial crack in the root region near where crack propagation was observed to initiate in tensile tests (Fig. 3).

More detailed characterisation was performed using (S)TEM of lamellae lifted out using FIB from eight locations along the Al-steel interface, as indicated in Fig. 7(a). Three characteristic interface appearances were identified; i) straight (e.g. Fig. 7(b)), ii) rough (e.g. Fig. 7(c)) and iii) wavy (e.g. Fig. 7(d)) interfaces. Straight interfaces were observed in lamellae from the top part of the joint (Lamellae $5-8$), and these interfaces showed either no signs of an IMP layer (Lamellae 6 and 7) or an IMP layer in only limited parts of the interface (Lamellae 5 and 8). Rough and wavy interfaces were observed in lamellae from the bottom region (Lamellae $1-4$), and these interfaces were covered by IMP layers that were discontinuous (Lamellae 1 and 2) or continuous (Lamellae 3 and 4). (S)TEM results from all lamellae are shown in SI S5.

Figs. 7(b)-(d) show Lamellae 3, 4 and 8 that displayed the three different interface appearances. Fig. 7(b) shows an overview bright-field (BF)-TEM image of Lamella 8 that displayed a straight interface. Lamella 8 was lifted out from the steel fracture surface of specimen R2 from a region where a thin and dimpled Al layer covered steel, which explains the top serrated Al surface seen in Fig. 7(b). A restricted IMP layer was found covering only a ~0.9 μm wide portion of the Al-steel interface, which is shown in the inset. Fig. 7(c) shows an overview BF-TEM image of Lamella 4 where a rough interface with deformed regions of intermixed Al and steel were seen. A ~40 nm thick IMP layer was observed over the whole interface, and the IMP layer grew around the deformed steel fragments near the interface, which can be seen in the insets in (c). In Fig. 7(d) an overview BF-TEM image of Lamella 3 is shown, where a slightly wavy Al-steel interface can be seen. The interface was continuously covered by a ~30 nm thick interfacial IMP layer. Further, the number density of dispersoids was observed by visual inspection to be higher close to the steel interface, relative to the number density ≳1 μm away from the interface.
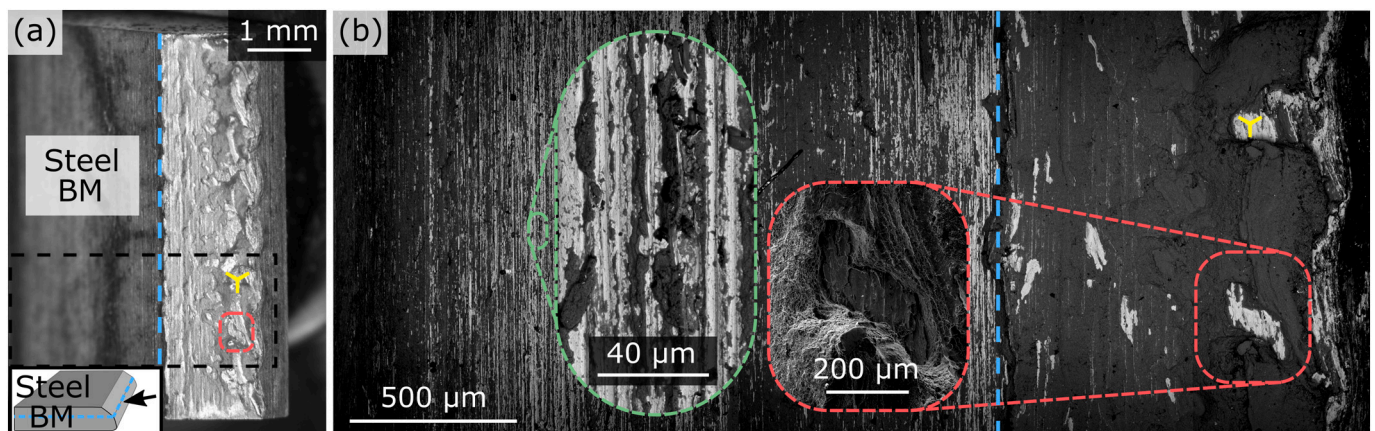

Fig. 4. The steel fracture surface resulting from tensile testing of specimen R2. (a) Optical micrograph. The bottom inset illustrates the viewing direction, and the blue lines indicate the boarder between the top and the bottom part of the fracture surface. (b) BSE SEM image where steel appears light grey and Al dark grey. The inset outlined in green displays a SE SEM image of residual Al found on the upper part of the steel, while that in red shows a SE SEM image of a dent in the residual Al. (For interpretation of the references to colour in this figure legend, the reader is referred to the web version of this article.)
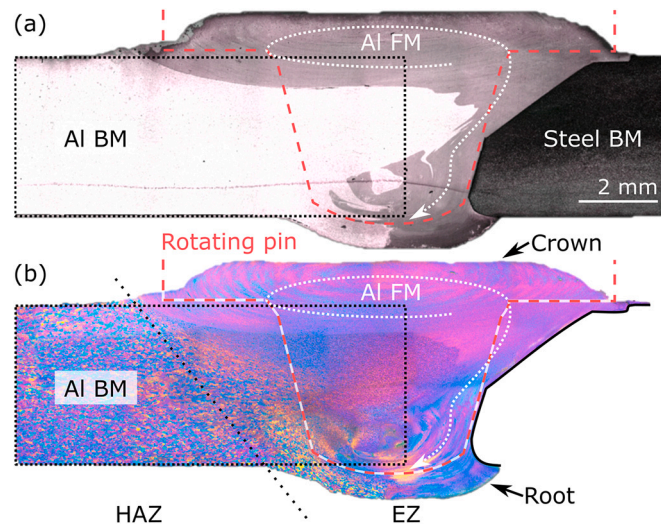
Fig. 5. Optical microscopy of joint cross-sections. (a) Micrograph where the steel BM appears dark grey, the FM medium grey and the Al BM light grey. The location of the Al BM plate before joining is marked by a black line, the flow of FM during joining is illustrated by a white curved arrow, and the rotating pin during joining is outlined in red. (b) Polarised light micrograph showing the Al grain structure. The locations of the root and crown regions, the heat affected zone (HAZ) and the extrusion zone (EZ) are indicated. (For interpretation of the references to colour in this figure legend, the reader is referred to the web version of this article.)
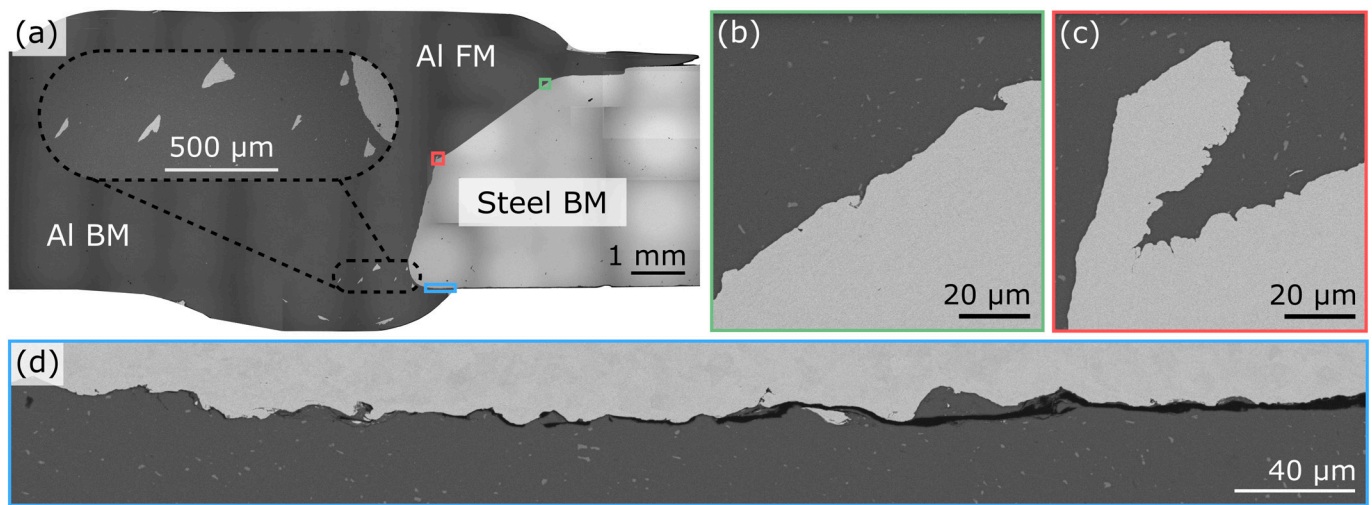

Fig. 6. BSE SEM images of the joint cross-section. (a) Overview of the weld region where the inset shows steel fragments in the extrusion zone. (b), (c) and (d) show higher magnification images of the green, red and blue regions marked in (a), respectively. (c) highlights a steel protrusion, while (d) emphasises a root crack. (For interpretation of the references to colour in this figure legend, the reader is referred to the web version of this article.)

3.2.2. The interfacial intermetallic phase layer

The chemical composition of the interfacial IMP layer was investigated by STEM EDS. The ~0.9 μm wide IMP layer in Lamella 8 is shown in Fig. 8, and the element maps in (c) reveal that the major constituents were Al, Fe and Si. In addition, the element maps show a discontinuous interfacial oxide layer, and it can be seen that the Al-Fe-Si layer grew into the Al side and was thicker near the gaps in the oxide layer. Also, some Mn-rich inclusions can be seen in steel, together with some N- and C-rich regions near the steel interface. Apart from the IMP layer segment shown in Fig. 8, Lamella 8 showed no signs of any interfacial Al-Fe(-Si) layer, and an interfacial oxide layer covered the remaining part of the interface. This interfacial oxide layer was ~5 nm thick and contained mainly Al, O, Mg and minor amounts of Si, as shown in SI S5.

Lamella 3 that had a continuous IMP layer was also investigated by STEM EDS, as shown in Fig. 9. It can be seen that dispersoids located close to the interface were primarily composed of Al-Mg-Si, Al-(Fe, Mn, Cr)-Si or Al-Si-Zr, whereas the IMP layer was composed of Al-Fe-Si-rich phases, as for Lamella 8. In addition, Al-O(-Mg)(-Si) oxide particles were seen near the IMP layer. The interfacial layers in the other lamella were also investigated by STEM EDS, as shown in SI S5. All showed indications of an interfacial Al-Fe-Si layer and/or of an interfacial Al-O-Mg-Si layer.

The IMP layer composition was estimated using STEM EDS data from Lamellae 3, 4 and 8, by summing spectra inside masked regions corresponding to the IMP layers, and performing model fitting and quantification of the sum spectra, as shown in SI S5. The resulting average relative composition and standard deviation for the major constituents was 59 ± 6 at.% Al, 32 ± 6 at.% Fe and 9 ± 1 at.% Si. These values were
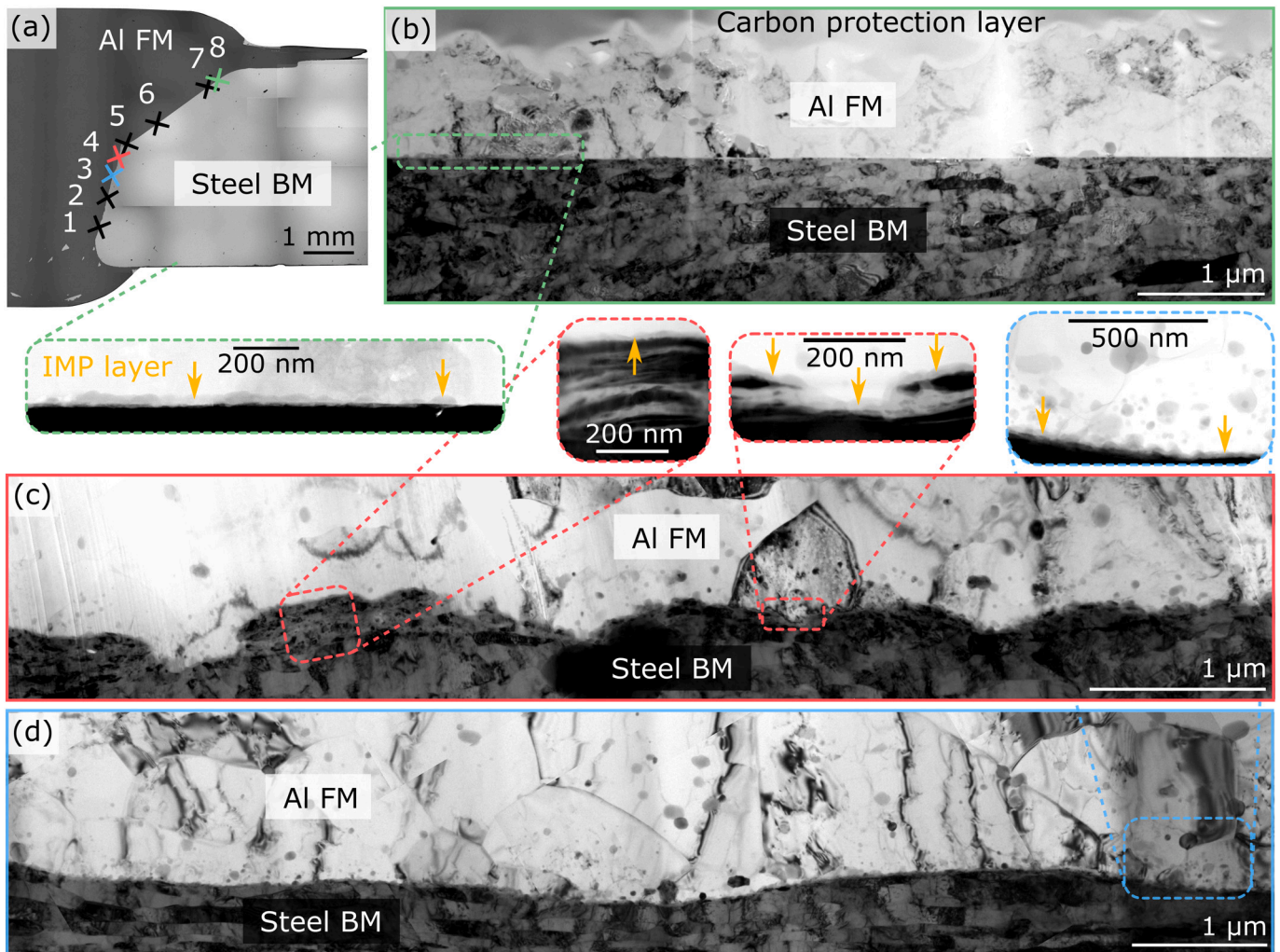
Fig. 7. TEM characterisation of the Al-steel interface region. (a) BSE SEM image showing the locations from where TEM lamellae were lifted out by FIB. (b) BF-TEM image of Lamella 8 showing a straight interface. The inset shows a BF-STEM image of a ~0.9 μm wide IMP layer segment. (c) BF-TEM image of Lamella 4 showing a rough interface region. The left-hand inset shows a BF-STEM image of intermixed Al and steel, while the right-hand inset shows an IMP layer growing around deformed steel fragments. (d) BF-TEM image of Lamella 3 showing a slightly wavy interface. The BF-STEM image inset shows a relatively large number of small dispersoids close to a continuous IMP layer.

subject to considerable errors due to overlap of the IMP layer with both steel and Al to different extent. In addition, absorption of low energy X-rays, i.e. Al-Kα and Si-Kα, caused the proportion of these elements to be systematically underestimated. Nevertheless, this rough estimation suggested that the IMP layer was composed primarily of Al-Fe(-Si) IMP (s) with $\gtrsim$9 at.% Si.

The distribution and morphology of IMP crystals, and the crystalline phases present in the IMP layer, were assessed using SED data from an interface region in Lamella 3. Fig. 10(a) shows a virtual bright-field (VBF) grayscale image, with overlayed coloured VDF image segments showing the morphologies of some individual interfacial IMP crystals and some dispersoids embedded in Al. Fig. 10(b) shows coloured diffraction spots corresponding to the coloured VDF segments in (a), and these are plotted on top of a grayscale pattern that shows the maximum intensity with respect to detector position based on all patterns from the region shown in (a). From Figs. 10(a) and (b) it can be seen that the IMP layer was polycrystalline and consisted of crystals with elliptical shapes, some nearly semi-elliptical with the straight side touching steel. The interfacial IMP crystals within the area shown in Fig. 10(a) had average dimensions of ~20 nm, including some crystals shorter than ~10 nm and some up to ~40 nm long.

To assess the crystal structure of the IMP crystals, diffraction patterns

from individual crystals were extracted from the SED data and compared against expected diffraction from candidate Al-Fe(-Si) crystal structures reported in literature [30–33]. Diffraction patterns recorded near major zone axes would be most useful for such phase categorisation, but in this case the small size of the IMP crystals made orienting individual crystals to such orientations infeasible. SED data were therefore recorded in a tilt series to increase the probability of recording data from some crystals oriented close to zone axes. Inter-vector distances were measured between recorded Bragg peaks and converted to average d-spacings, which were then compared to calculated values for all candidate Al-Fe(-Si) phases. Crystallographic information for all candidates is given in SI S6. In Fig. 10(c), d-spacings are plotted for a subset of the candidate phases, including only Al-rich candidate Al-Fe(-Si) phases reported on Al-steel interfaces [34–36]; θ-Fe$_4$Al$_{13}$ (also referred to as FeAl$_3$ or Fe(Al, Si)$_3$) [37], cubic α_c-Al-Fe-Si (Al$_{15}$(Fe,Mn)$_3$Si$_2$) [38], hexagonal α_h-Al$_{7.1}$Fe$_2$Si (τ_5) [39], and β-Al$_{4.5}$FeSi (τ_6) [40]. Plots that include all candidates and that cover larger ranges of d-spacings are shown in SI S7. The most commonly measured larger d-spacings were ~8.8 Å and ~6.2 Å, which fit several candidates, including in particular the α_c phase (d_{110} = 8.9 Å and d_{200} = 6.3 Å). Based on the measured d-spacings alone, it was not possible to determine the IMP(s) present.

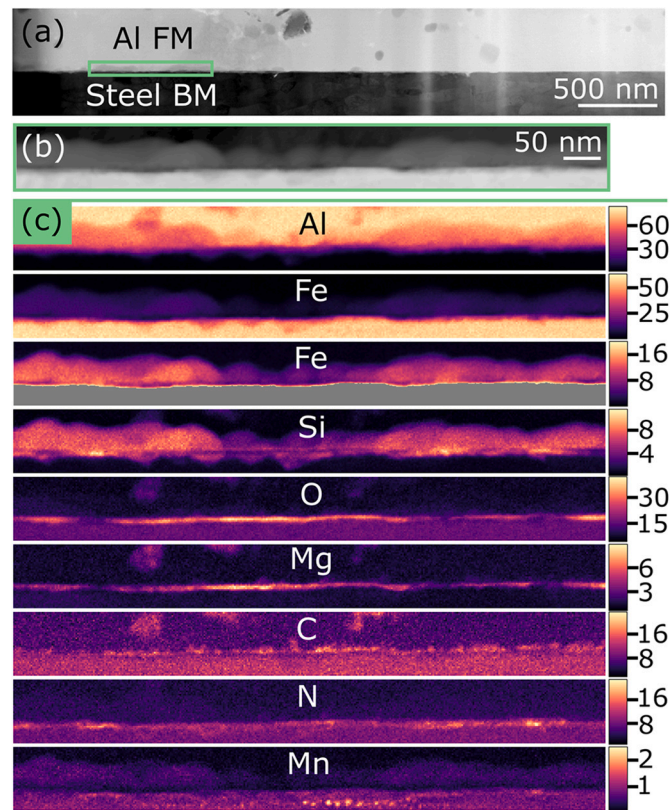Finally, selected patterns recorded near major crystallographic zone

Fig. 8. STEM of the restricted IMP layer in Lamella 8. (a) BF-STEM overview image. (b) HAADF-STEM image and (c) element maps (showing at.%) based on STEM EDS of the region highlighted in (a). Note that two Fe maps are shown, and that the bottom one displays only low amounts of Fe ($0 - 20$ at.%).

axes were indexed with respect to the candidate Al-Fe(-Si) phases. For each selected pattern, the two longest average d-spacings corresponding to non-parallel rows of spots, together with the angle between them, were considered, and all candidates were checked for possible zone axis giving spots matching these. Several individual patterns could be indexed with respect to the α_c phase, as shown in Figs. 10(d)-(f), as could some diffraction patterns from dispersoids embedded in the Al FM. This suggested that the α_c phase was the most probable IMP candidate in the interfacial layer. However, some d-spacings (e.g. 10.8 Å and 7.8 Å), and several individual patterns could not be indexed with respect to this phase, which suggested that additional phase(s) were present. SI S7 shows the considered selected patterns.

4. Discussion

4.1. Joint strength

The UTS of the second generation HYB Al-steel butt joint presented here ($184 - 220$ MPa) surpassed the UTS of the first generation ($104 - 140$ MPa [16]). The relatively large spread in these values may be explained by local fluctuations in the FM supply and placement of the

pin during joining, which may lead to local variations in bonding conditions. The strength increase may be understood by considering the differences between the setups used for the first and second generation HYB joining, which are illustrated in Figs. 11(a) and (b). There are two main differences. Firstly, the shape of the steel groove was different, with the first generation having a half V-form and the second a half Y-form. Secondly, the steel was placed on the RS in the first generation, while on the AS in the second. This change is consistent with the standard practice of placing the hardest material on the AS for FSW butt joints [5,6]. The material on the AS experiences larger shear forces, which was expected to give better Al-steel bonding.

The Al BM and FM were both notably affected by the joining process. The horizontal hardness profile (Fig. 2(a)) showed a typical HAZ with a continuous hardness decrease towards the weld centre. Such a HAZ was expected since the Al BM was artificially aged before joining to reach peak hardness condition that is characterised by a high number density of nanoscale hardening precipitates. Upon heating to ≳200°C during joining, coarsening and dissolution of hardening precipitates, possibly accompanied by re-precipitation of non-hardening phases, were expected to leave the Al BM in an overaged state with lower hardness, in accordance with studies of FSW joints of aged 6xxx Al alloys [41–43].
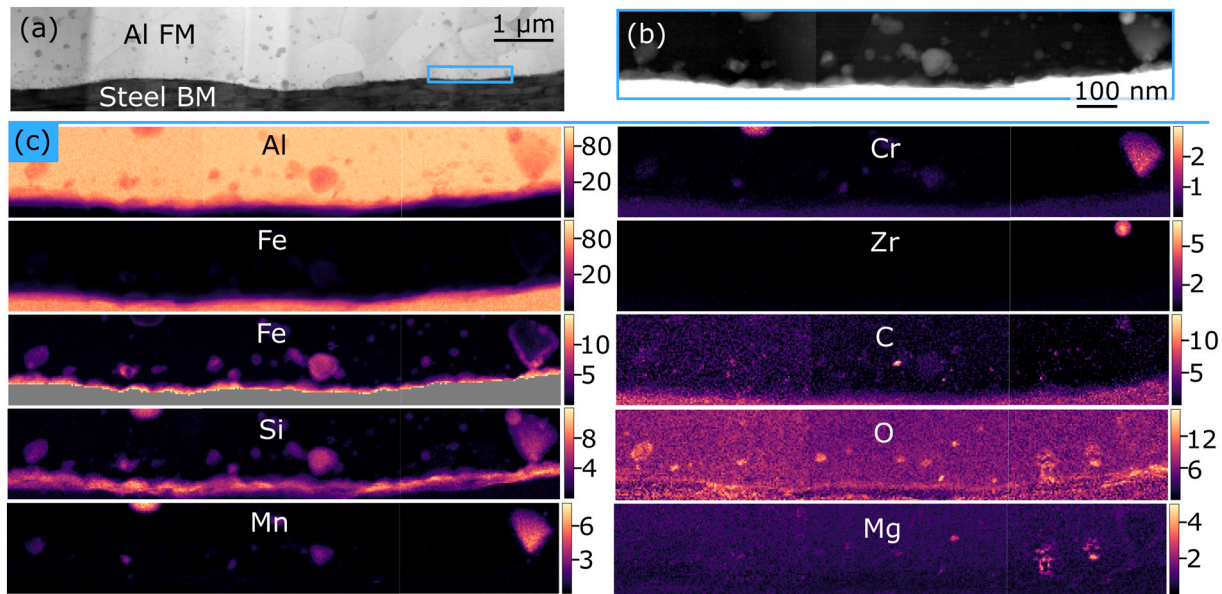
Fig. 9. STEM of the interfacial IMP layer in Lamella 3. (a) BF-STEM overview image. (b) HAADF-STEM image and (c) element maps (showing at.%) based on STEM EDS of the region highlighted in (a). Note that two Fe maps are shown, and that the bottom one displays only low amounts of Fe (0 − 15 at.%). All displayed maps comprise results from three datasets acquired individually.
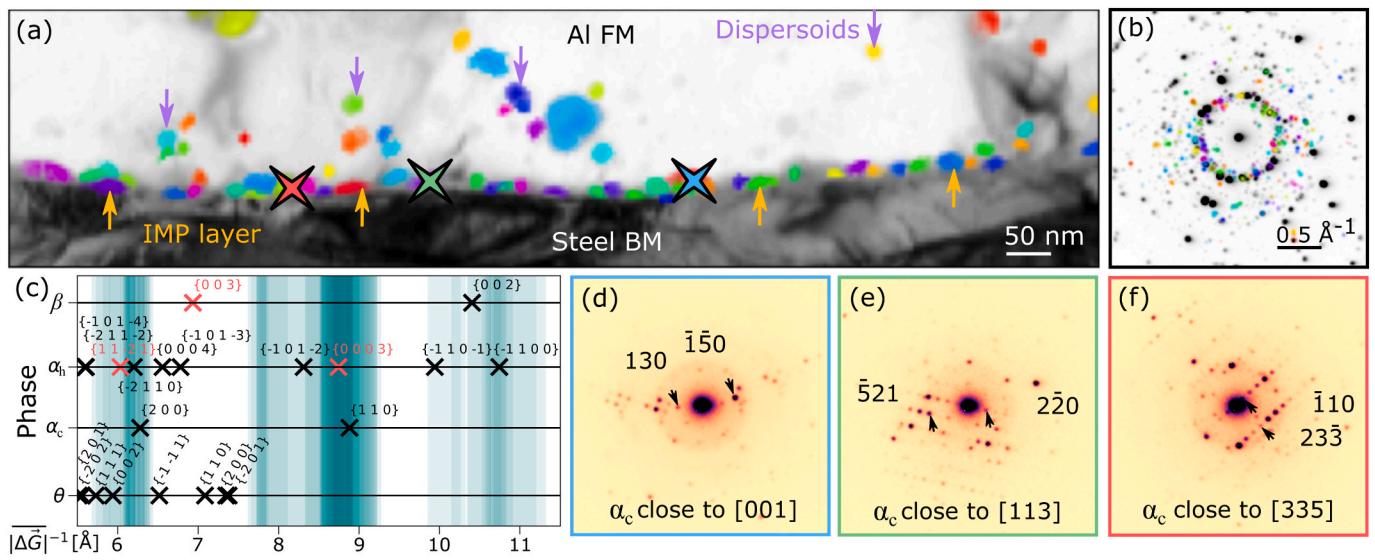

Fig. 10. Scanning electron diffraction of an interface region in Lamella 3 (the same as Fig. 9). (a) Virtual bright field image with overlayed coloured virtual dark field image segments from some individual crystals in the IMP layer and some dispersoids in the Al FM. (b) Coloured diffraction spots corresponding to the coloured segments in (a), superimposed on a greyscale pattern that shows the maximum intensity with respect to detector position based on all patterns from the region in (a). (c) Measured average d-spacings from selected patterns in the IMP layer plotted in partly transparent turquoise with a line width equal to one standard deviation. On the vertical axis, d-spacings of the phases θ, α_c, α_h and β are shown. Black crosses correspond to kinematically allowed spots, while red crosses correspond to spots possibly seen due to double diffraction. Patterns indexed with respect to the α_c phase from crystals oriented close to (d) [001], (e) [113] and (f) [335] zone axis, located at the positions marked in (a). (For interpretation of the references to colour in this figure legend, the reader is referred to the web version of this article.)

The hardness decrease continued until a minimum was reached near the EZ-HAZ boarder, which coincided with the strain development in the Al BM during tensile testing (Fig. 3(c)). After this point, the horizontal hardness profile showed increasing values towards the weld centre (Fig. 2(a)). Such an increase has also been seen in FSW joints, where it was coupled to increasing dissolution of non-hardening precipitates leaving increasing amounts of solutes in solid solution, which in turn gave increasing hardness during natural ageing after cooling [41,44]. However, a hardness decrease was seen in the vertical profile (Fig. 2(a)) moving from the weld crown, that was primarily composed of the harder FM, towards the root region, where mixing of the Al BM and FM

occurred (Fig. 5(a)). The FM was richer in dispersoid forming elements (Mn, Cr and Zr) and was before joining thermo-mechanically processed to promote work hardening and formation of fine dispersoids. During joining, both the FM and the Al BM in the EZ were subjected to extensive deformation and heating, resulting in a complex microstructure (Fig. 5 (b)). Small equiaxed grains were seen in the central region and onion-ring structures were seen at the top, both of which are common in FSW joining [18,43]. However, larger grains reflecting the Al flow were seen towards the root region, which indicated higher heat inputs. Studies focused on the Al region are required for further insight into the precipitation phenomena and microstructural features responsible for
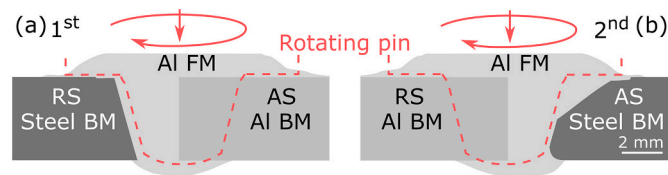
Fig. 11. Illustration of the setup used for the production of (a) first and (b) second generation (this work) HYB Al-steel joints, where the steel BM is placed on the retreating side (RS) or the advancing side (AS), respectively. The outline of the rotating pin during joining is indicated with a red dashed line, and its movement is indicated with red arrows. (For interpretation of the references to colour in this figure legend, the reader is referred to the web version of this article.)

the hardness variations in the Al region.

Despite the softening on the Al side, cracks in the root region lead to final fracture along the Al-steel interface for all specimens. Poor bonding in the root region was connected to the shape of the steel groove. The very bottom of the bevelled steel edge created a pit filled with FM underneath the steel plate. Considering the Al flow during joining (Fig. 5), the forces acting in this region were modest, resulting in poor bonding and formation of root cracks. The forces were also modest for the top part of the steel plate, where the FM flowed outward over the steel plate without meeting any obstacle, giving lack of bonding. However, the fracture surfaces indicated that the Al-steel bonding in the bottom half of the joint was sufficiently strong, except for in the root region. The wavy pattern in the Al on the fracture surfaces (Fig. 4), that resembled an impression of the extrusion dies in the pin, suggested that the weakest part in the bottom region was not the Al-steel interface, but rather the bonding between new and previously deposited Al as the pin traversed the weld groove. This indicated that sufficient Al-steel bonding was achieved in regions that experienced high pressure. For development of future generations of HYB Al-steel butt joints, modifying the pin and steel groove shape to increase the pressure in the root region, should be investigated.

The HYB joint performed comparably, in terms of UTS, to sound Al-steel butt joints made with the similar Al alloy 6061 as BM using other joining techniques. For instance, FSW joints have reached ca. 250 MPa [45] and ca. 240 MPa [35], while laser-assisted FSW joints have demonstrated UTS values of ca. 196 MPa [46] and laser welding-brazing joints have demonstrated ca. 208 MPa [47]. Investigations into the bonding mechanisms were crucial to explain the origin of the considerable bond strength.

4.2. Bonding mechanisms

The Al-steel interface was investigated by SEM and (S)TEM in order to explain the bonding mechanisms induced by HYB. Signs of bonding were seen on both the micro- and nanoscale. On the microscale, SEM studies of the joint cross-section (Fig. 6) showed that a significant portion of the interface was rough with small hook-like features. The larger surface area associated with a rough interface is typically beneficial for bond strength. Further, features where one material has flowed into protrusions on the opposing material surface, indicate mechanical interlocking. These micro-interlock features were similar to those observed in FSW Al-steel joints, which were suggested to enhance the bond strength [48]. On the nanoscale, (S)TEM studies uncovered layered intermixed Al-steel regions (Fig. 7(c)). These regions were similar to swirl-like intercalated layers reported in FSW joints, that were attributed to the large plastic deformation induced by the stirring of the tool [49].

An interfacial Al-Fe-Si IMP layer (Figs. 9 and 10) that was discontinuous and $10 - 50$ nm thick was revealed by (S)TEM investigations. IMP layers may govern the tensile strength of Al-steel joints based primarily on the layer thickness [1–4]. A thicker layer may lead to fracture along the Al-steel interface and a decrease in tensile strength, due to the inherent brittleness of the IMPs and/or due to porosity formed during IMP growth [3]. For instance, one study found that the FSW joint strength decreased exponentially with increasing IMP layer thickness, e. g. the joint strength decreased from 327 MPa to 205 MPa when the IMP layer thickness increased from 0.11 µm to 0.34 µm [2]. In another study on FSW joints, fracture occurred in Al and the tensile strength was $\gtrsim$250 MPa when the IMP layer thickness was below ~0.5 µm, while fracture occurred in the IMP layer yielding a strength of $\lesssim$100 MPa when the IMP layer thickness exceeded ~2 µm [4]. In this context, the $10 - 50$ nm thick layer observed here was considered thin. Similar nanoscale IMP layers have been reported in a few other studies. For instance, a 30 nm thick discontinuous IMP layer was found in a FSW joint after post-joining heat treatment at 400°C for 9 min [3], and a polycrystalline non-uniform $40 - 70$ nm thick IMP layer with ~5 at.% Si was found in a friction stir dovetail joint [50], which highly resembled the IMP layer found here. Generally, thinner IMP layers form with decreasing heat input, since growth of IMP layers typically is diffusion controlled [51]. The joint temperature during HYB joining has been assumed to reach a maximum of ~400°C, and considering the resulting thermal profile, a nanoscale IMP layer can be expected for HYB joints [15]. Furthermore, the Al FM contained Si, which can be beneficial as it may lead to a reduction of the IMP layer growth rate [34,36,52–54]. Thus, it was believed that the low HYB process temperature and favourable Al FM composition, made it possible to avoid excessive IMP growth and to achieve substantial bond strength.

Analysis of SED data indicated that the polycrystalline IMP layer contained the cubic α_c phase (Fig. 10). Based on literature, Al-rich IMPs were expected to form first on Al-Fe interfaces, specifically θ-Fe_4Al_{13} for low Si contents, and α_h-$Al_{7.1}Fe_2Si$ and β-$Al_{4.5}FeSi$ for higher Si contents [34,55]. However, the cubic α_c phase generally forms at the expense of the hexagonal α_h phase in the presence of small amounts of certain transition elements, e.g. Mn and Cr [56–58], and these were contained in the FM used here. The roughly estimated Si content of $\gtrsim$9 at.% (Fig. 9) was consistent with Si contents in the range of $6 - 11$ at.% previously reported for α_c-Al-(Fe,Mn)-Si crystals [59]. The α_c phase has also been found on Al-steel interfaces in other studies [36,60], and in an early study a cubic Fe_3SiAl_{12} phase highly similar to α_c was reported to form at $\gtrsim$350°C [53], which further supported the presence of α_c. Al-(Fe, Mn, Cr)-Si dispersoids in the Al FM were also identified as α_c phases (SI S7). Some regions showed indications of a higher dispersoid number density near the Al-steel interface (Fig. 9), which was also reported in another study [50]. Some dispersoids contained increasing amounts of Fe towards their edges (Fig. 9), consistent with previous work explaining this based on Fe diffusing more slowly into the dispersoids during prolonged growth [61]. Here it was possible that Fe diffusion across the Al-steel interface during HYB promoted formation of small dispersoids in parallel to growth of already formed dispersoids. However, dispersoid statistics was outside the scope of this study, and future studies of large

areas would have to be done to reach valid conclusions. In any case, α_c could not explain all the diffraction recorded from the IMP layer, which indicated that α_c likely co-existed with (an)other Al-Fe(-Si) phase(s) that could not be identified. Further investigations are necessary to fully understand the IMP formation and growth on Al-steel interfaces at nanoscale.

Regions with an interfacial Al-Fe-Si layer demonstrated bonding via interdiffusion. However, some regions showed a ~5 nm thick Al-O-Mg-Si layer (Fig. 8 and SI S5). This layer resembled the Al_2O_3 layer, that may also contain Mg and Si, typically found on Al surfaces exposed to air [62–64]. In Al joining, it is generally believed that breaking up the native oxide layer and allowing fresh metal to meet, promotes metallurgical bond formation [65]. Here, Al was heavily deformed and the native surface layer presumably disintegrated and was dragged into the EZ during HYB, similar to in FSW where oxide layer remnants can be found as dispersed particles in the stir zone [66,67]. The nanoscale Al-O-Mg-Si layer seen on the Al-steel interface supposedly formed as a result of air access during the Al FM extrusion in HYB. Nanoscale Al-O(-Mg)(-Si) oxide films have also been found on extruded Al profiles [68] and at Al-steel interfaces in FSW joints [69–71]. Further, it was seen that the Al-Fe-Si layer may grow thicker into Al where there are gaps in the oxide layer (Fig. 8), consistent with the general belief that an oxide film may act as an interdiffusion barrier [72,73]. Previous studies of Al-steel joints have reported both interfacial oxide layers that were coupled to interfacial fracture [70] or conversely, to high bond strength [69,71,73]. Here, interfacial Al-O-Mg-Si layers were also seen in regions where Al stuck to steel after tensile testing, which suggested that limited interface regions covered by interfacial oxides formed during joining not necessarily have detrimental effects on the overall bond strength. Further studies are needed to determine the role of nanoscale interfacial oxides in Al-steel joints made in the solid state.

By combining the findings from the microscopy investigations with those from the mechanical testing, regions with low and high relative bond strength could be identified, as illustrated in Fig. 12. The lamellae that showed flat interface appearances with no or only a restricted IMP layer, were predominantly from the top half of the joint. The steel fracture surface (Fig. 4) showed less residual Al in this region, which indicated limited bonding. On the other hand, a large amount of residual Al was found on the bottom half of the steel fracture surface, which hinted to stronger Al-steel bonding. Also, the bottom half showed a rougher interface with more interlocking signs, and the TEM lamellae that showed clear signs of a nanoscale IMP layer were also from the same region. Thus, in total the presented characterisation indicated that stronger Al-steel bonding was achieved for interface regions that displayed both a nanoscale IMP layer and more interlocking features. This is supported by another study, where the isolated and combined effects of a large mechanical interlock and a thin IMP layer were investigated, and where it was found that the highest bond strength was achieved when both of these were present simultaneously [50].

5. Summary and conclusions

A second generation Al-steel HYB butt joint was subjected to microstructural and mechanical characterisation, from which the main findings can be summarised as follows.

i. Transverse hardness profiles showed a heat affected zone that extended 13.5 mm into Al, while steel was unaffected.

ii. The ultimate tensile strength (UTS) was measured to be in the range of $184 - 220$ MPa, corresponding to $60 - 72\%$ joint efficiency.

iii. Digital image correlation (DIC) analysis of the strain development during tensile testing showed that although strain developed in the soft zone in Al, cracks in the root region were severe. The final fracture propagated from root cracks and ran close to the Al-steel interface.
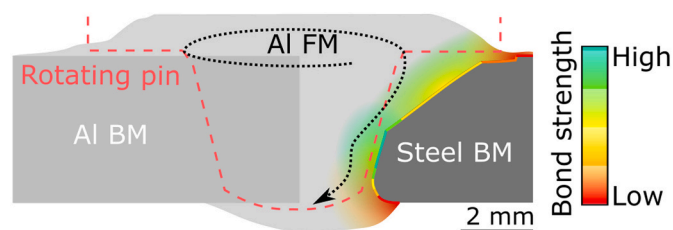

Fig. 12. Simplified qualitative illustration of the bond strength in the investigated joint. The Al-steel interface is coloured according to low (red) to high (turquoise) relative bond strength. The position of the Al BM plate before joining is marked by a medium grey rectangle, the flow of FM during joining is illustrated by a black curved arrow, and the rotating pin during joining is indicated by a red line. (For interpretation of the references to colour in this figure legend, the reader is referred to the web version of this article.)

iv. Scanning electron microscopy (SEM) of the fracture surfaces revealed significant portions of residual Al on the steel fracture surface, which indicated sufficient Al-steel bond strength, especially on the bottom half of the steel that experienced larger pressure during joining.

v. SEM and transmission electron microscopy (TEM) investigations revealed signs of microscale mechanical interlocking, showed that the Al-steel interface was rough, especially on the bottom half of the steel, and showed some intermixed Al-steel regions.

vi. TEM characterisation showed an interfacial discontinuous $10 - 50$ nm thick intermetallic phase (IMP) layer. Quantification by X-ray energy dispersive spectroscopy (EDS) indicated that the layer was mainly composed of Al, Fe and Si with a relative Si content roughly estimated to $\gtrsim 9$ at.%. Some regions showed ~5 nm thick interfacial oxide layers mainly composed of Al, O and Mg with minor amounts of Si.

vii. Analysis of scanning electron diffraction (SED) data acquired in a tilt series indicated that the IMP layer was polycrystalline with nanocrystals of the cubic α_c phase. The α_c phase could not explain all the diffraction patterns from the Al-Fe-Si layer, and further investigations are needed to fully understand the Al-Fe(-Si) phase formation at the nanoscale in Al-steel joints.

In short, the Al-steel HYB butt joint showed considerable bond strength that was attributed to a combination of microscale mechanical interlocking and a nanoscale interfacial Al-Fe-Si layer.

Data availability

The raw SED data have been made available [74].

Declaration of Competing Interest

None.

Acknowledgements

Appendix A. Supplementary data

Supplementary data to this article can be found online at https://doi.org/10.1016/j.matchar.2020.110761.

References

[1] R. Borrisutthekul, T. Yachi, Y. Miyashita, Y. Mutoh, Suppression of intermetallic reaction layer formation by controlling heat flow in dissimilar joining of steel and aluminum alloy, Mater. Sci. Eng. A 467 (1–2) (2007) 108–113, https://doi.org/10.1016/j.msea.2007.03.049.

[2] T. Tanaka, T. Morishige, T. Hirata, Comprehensive analysis of joint strength for dissimilar friction stir welds of mild steel to aluminum alloys, Scr. Mater. 61 (7) (2009) 756–759, https://doi.org/10.1016/j.scriptamat.2009.06.022.

[3] H. Springer, A. Kostka, J.F. dos Santos, D. Raabe, Influence of intermetallic phases and Kirkendall-porosity on the mechanical properties of joints between steel and aluminium alloys, Mater. Sci. Eng. A 528 (13–14) (2011) 4630–4642, https://doi.org/10.1016/j.msea.2011.02.057.

[4] R. Hatano, T. Ogura, T. Matsuda, T. Sano, A. Hirose, Relationship between intermetallic compound layer thickness with deviation and interfacial strength for dissimilar joints of aluminum alloy and stainless steel, Mater. Sci. Eng. A 735 (2018) 361–366, https://doi.org/10.1016/j.msea.2018.08.065.

[5] W. Cai, G. Daehn, A. Vivek, J. Li, H. Khan, R.S. Mishra, M. Komarasamy, A state-of-the-art review on solid-state metal joining, J. Manuf. Sci. Eng. Trans. ASME 141 (3) (2019) 1–35, https://doi.org/10.1115/1.4041182.

[6] K. Kimapong, T. Watanabe, Friction stir welding of aluminum alloy to steel, Weld. J. (Miami, Fla) 83 (10) (2004) 277–282 (issn: 00432296).

[7] H. Laukant, C. Wallmann, M. Müller, M. Korte, B. Stirn, H.G. Haldenwanger, U. Glatzel, Fluxless laser beam joining of aluminium with zinc coated steel, Sci. Technol. Weld. Join. 10 (2) (2005) 219–226, https://doi.org/10.1179/174329305X37051.

[8] M. Merklein, A. Giera, Laser assisted friction stir welding of drawable steel-aluminium tailored hybrids, Int. J. Mater. Form. 1 (2008) 1299–1302, https://doi.org/10.1007/s12289-008-0141-x.

[9] Ø. Grong, Recent advances in solid-state joining of aluminum, Weld. J. 91 (1) (2012) 26–33.

[10] U.R. Aakenes, Industrialising of the hybrid metal extrusion & bonding (HYB) method from prototype towards commercial process, PhD thesis,, Norwegian University of Science and Technology, 2013 (isbn: 9788247148198).

[11] U.R. Aakenes, Ø. Grong, T. Austigard, Application of the hybrid metal extrusion & bonding (HYB) method for joining of AA6082-T6 base material, Mater. Sci. Forum 794-796 (2014) 339–344, https://doi.org/10.4028/www.scientific.net/MSF.794-796.339.

[12] J. Blindheim, T. Welo, M. Steinert, First demonstration of a new additive manufacturing process based on metal extrusion and solid-state bonding, Int. J. Adv. Manuf. Technol. 105 (5–6) (2019) 2523–2530, https://doi.org/10.1007/s00170-019-04385-8.

[13] J. Blindheim, Ø. Grong, T. Welo, M. Steinert, On the mechanical integrity of AA6082 3D structures deposited by hybrid metal extrusion & bonding additive manufacturing, J. Mater. Process. Technol. 282 (2020), https://doi.org/10.1016/j.jmatprotec.2020.116684.

[14] Ø. Grong, L. Sandnes, F. Berto, A status report on the hybrid metal extrusion & bonding (HYB) process and its applications, Mater. Des. Process. Commun. 1 (2) (2019), https://doi.org/10.1002/mdp2.41 e41.

[15] Ø. Grong, L. Sandnes, T. Bergh, P.E. Vullum, R. Holmestad, F. Berto, An analytical framework for modelling intermetallic compound (IMC) formation and optimising bond strength in aluminiumsteel welds, Mater. Des. Process. Commun. (2019), https://doi.org/10.1002/mdp2.57 no. February, e57.

[16] F. Berto, L. Sandnes, F. Abbatinali, O. Grong, P. Ferro, Using the hybrid metal extrusion & bonding (HYB) process for dissimilar joining of AA6082-T6 and S355, Proc. Struct. Integr. 13 (2018) 249–254, https://doi.org/10.1016/j.prostr.2018.12.042.

[17] Ø. Grong, Method and devices for joining of metal components, particularly light metal components, US patent, US 7131567 (2006) B2.

[18] P.L. Threadgill, A.J. Leonard, H.R. Shercliff, P.J. Withers, Friction stir welding of aluminium alloys, Int. Mater. Rev. 54 (2) (2009) 49–93, https://doi.org/10.1179/174328009X411136.

[19] Ø. Grong, L. Sandnes, F. Berto, Progress in solid state joining of metals and alloys, Proc. Struct. Integr. 17 (2019) 788–798, https://doi.org/10.1016/j.prostr.2019.08.105.

[20] F. Leoni, Ø. Grong, L. Sandnes, T. Welo, F. Berto, Finite element modelling of the filler wire feeding in the hybrid metal extrusion & bonding (HYB) process, J. Adv. Join. Process. 26 (2020) 321–329, https://doi.org/10.1016/j.jajp.2020.100006.

[21] ASTM International, ASTM E8/E8M - 16a Standard test methods for tension testing of metallic materials, 2016, https://doi.org/10.1520/E0008_E0008M-16A.

[22] E. Fagerholt, E. Østby, T. Børvik, O.S. Hopperstad, Investigation of fracture in small-scale SENT tests of a welded X80 pipeline steel using digital image correlation with node splitting, Eng. Fract. Mech. 96 (2012) 276–293, https://doi.org/10.1016/j.engfracmech.2012.08.007.

[23] E. Fagerholt, T. Borvik, O.S. Hopperstad, Measuring discontinuous displacement fields in cracked specimens using digital image correlation with mesh adaptation and crack-path optimization, Opt. Lasers Eng. 51 (3) (2013) 299–310, https://doi.org/10.1016/j.optlaseng.2012.09.010.

[24] L.J. Barker, Revealing the grain structure of common aluminium alloy metallographic specimens, Trans. A.S.M. 42 (1950) 347–356.

[25] F. de la Peña, E. Prestat, V.T. Fauske, P. Burdet, P. Jokubauskas, M. Nord, T. Ostasevicius, K.E. MacArthur, M. Sarahan, D.N. Johnstone, J. Taillon, J. Lähnemann, V. Migunov, A. Eljarrat, J. Caron, T. Aarholt, S. Mazzucco, M. Walls, T. Slater, F. Winkler, B. Pquinn-Dls, G. Donval Martineau, R. McLeod, E. R. Hoglund, I. Alxneit, D. Lundeby, T. Henninen, L.F. Zagonel, A. Garmannslund, hyperspy/hyperspy: HyperSpy v1.5.2, Zenodo, 2019, https://doi.org/10.5281/ZENODO.3396791.

[26] D.N. Johnstone, P. Crout, J. Laulainen, S. Høgås, B. Martineau, T. Bergh, S. Smeets, S. Collins, J. Morzy, H.W. Ånes, E. Prestat, T. Doherty, T. Ostasevicius, D. Mohsen, E. Opheim, R. Tovey, E. Jacobsen, pyxem/pyxem: pyxem 0.10.1, Zenodo, 2020, https://doi.org/10.5281/ZENODO.3667613.

[27] T. Bergh, D.N. Johnstone, P. Crout, S. Høgås, P.A. Midgley, R. Holmestad, P. E. Vullum, A.T.J van Helvoort, Nanocrystal segmentation in scanning precession electron diffraction data, J. Microsc. 279 (3) (2020) 158–167, https://doi.org/10.1111/jmi.12850.

[28] B.H. Martineau, D.N. Johnstone, A.T.J. van Helvoort, P.A. Midgley, A.S. Eggeman, Unsupervised machine learning applied to scanning precession electron diffraction data, Adv. Struct. Chem. Imaging 5 (1) (2019) https://doi.org/10.1186/s40679-019-0063-3.

[29] L. Sandnes, Ø. Grong, J. Torgersen, T. Welo, F. Berto, Exploring the hybrid metal extrusion and bonding process for butt welding of AlMgSi alloys, Int. J. Adv. Manuf. Technol. 98 (5–8) (2018) 1059–1065, https://doi.org/10.1007/s00170-018-2234-0.

[30] C.M. Allen, K.A. O'Reilly, B. Cantor, P.V. Evans, Intermetallic phase selection in 1XXX A1 alloys, Prog. Mater. Sci. 43 (2) (1998) 89–170, doi: 10.1016 / S0079 - 6425(98)00003–6.

[31] N. Krendelsberger, F. Weitzer, J.C. Schuster, On the reaction scheme and liquidus surface in the ternary system Al-Fe-Si, Metall. Mater. Trans. A 38 (August) (2007), https://doi.org/10.1007/s11661-007-9182-x.

[32] G. Ghosh, Aluminim-iron-silicon. Iron systems, Part 1, SpringerMaterials Landolt-Börnstein - Group IV Physical Chemistry 11D1, 2008, pp. 1–83, https://doi.org/10.1007/978-3-540-69761-9_11.

[33] M.C.J. Marker, B. Skolyszewska-Kühberger, H.S. Effenberger, C. Schmetterer, K. W. Richter, Intermetallics phase equilibria and structural investigations in the system Al-Fe-Si, Intermetallics 19 (12) (2011) 1919–1929, https://doi.org/10.1016/j.intermet.2011.05.003.

[34] H. Springer, A. Kostka, E.J. Payton, D. Raabe, A. Kaysser-Pyzalla, G. Eggeler, On the formation and growth of intermetallic phases during interdiffusion between low-carbon steel and aluminum alloys, Acta Mater. 59 (4) (2011) 1586–1600, https://doi.org/10.1016/j.actamat.2010.11.023.

[35] T. Chen, Process parameters study on FSW joint of dissimilar metals for aluminum-steel, J. Mater. Sci. 44 (10) (2009) 2573–2580, https://doi.org/10.1007/s10853-009-3336-8.

[36] L.A. Jacome, S. Weber, A. Leitner, E. Arenholz, J. Bruckner, H. Hackl, A.R. Pyzalla, Influence of filler composition on the microstructure and mechanical properties of steel - aluminum joints produced by metal arc joining, Adv. Eng. Mater. 11 (5) (2009) 350–358, https://doi.org/10.1002/adem.200800319.

[37] J. Grin, U. Burkhardt, M. Ellner, K. Peters, Refinement of the Fe4Al13 structure and its relationship to the quasihomological homeotypical structures, Z. Krist. 209 (6) (1994) 479–487, https://doi.org/10.1524/zkri.1994.209.6.479.

[38] M. Cooper, The crystal structure of the ternary alloy α (AlFeSi), Acta Crystallogr. 23 (1967) 1106–1107, https://doi.org/10.1107/S0365110X67004372.

[39] R.N. Corby, P.J. Black, The structure of α- (AlFeSi) by anomalous-dispersion methods, Acta Crystallogr. B33 (1977) 3468–3475, https://doi.org/10.1107/S0567740877011224.

[40] V. Hansen, B. Hauback, M. Sundberg, C. Rømming, J. Gjønnes, β-Al$_{4.5}$FeSi: a combined synchrotron powder diffraction, electron diffraction, high-resolution electron microscopy and single-crystal X-ray diffraction study of a faulted structure, Acta Crystallogr. B 54 (4) (1998) 351–357, https://doi.org/10.1107/S0108768197017047.

[41] O.R. Myhr, Ø. Grong, Process modelling applied to 6082-T6 aluminium weldments II. Applications of model, Acta Metall. Mater. 39 (1) (1991) 2703–2708.

[42] Y.S. Sato, H. Kokawa, M. Enomoto, S. Jogan, Microstructural evolution of 6063 aluminum during friction-stir welding, Metall. Mater. Trans. A 30 (9) (1999) 2429–2437, https://doi.org/10.1007/s11661-999-0251-1.

[43] L.-E. Svensson, L. Karlsson, H. Larsson, B. Karlsson, M. Fazzini, J. Karlsson, Microstructure and mechanical properties of friction stir welded 5083 and 7075 aluminum alloys, Sci. Technol. Weld. Join. 5 (2000) 285–296, https://doi.org/10.1007/s11665-017-2543-8.

[44] Ø. Frigaard, Ø. Grong, O.T. Midling, A process model for friction stir welding of age hardening aluminum alloys, Metall. Mater. Trans. A 32 (5) (2001) 1189–1200, https://doi.org/10.1007/s11661-001-0128-4.

[45] E. Taban, J.E. Gould, J.C. Lippold, Dissimilar friction welding of 6061-T6 aluminum and AISI 1018 steel: properties and microstructural characterization, Mater. Des. 31 (5) (2010) 2305–2311, https://doi.org/10.1016/j.matdes.2009.12.010.

[46] X. Fei, X. Jin, Y. Ye, T. Xiu, H. Yang, Effect of pre-hole offset on the property of the joint during laser-assisted friction stir welding of dissimilar metals steel and aluminum alloys, Mater. Sci. Eng. A 653 (2016) 43–52, https://doi.org/10.1016/j.msea.2015.11.101.

[47] H. Xia, X. Zhao, C. Tan, B. Chen, X. Song, L. Li, Effect of Si content on the interfacial reactions in laser welded-brazed Al/steel dissimilar butted joint, J. Mater. Process. Technol. 258 (2018) 9–21, https://doi.org/10.1016/j.jmatprotec.2018.03.010.

[48] S. Lan, X. Liu, J. Ni, Microstructural evolution during friction stir welding of dissimilar aluminum alloy to advanced high-strength steel, Int. J. Adv. Manuf. Technol. 82 (9–12) (2016) 2183–2193, https://doi.org/10.1007/s00170-015-7531-2.

[49] W.-B. Lee, M. Schmuecker, A. Mercardo, G. Biallas, S.-B. Jung, Interfacial reaction in steelaluminum joints made by friction stir welding, Scr. Mater. 55 (2006) 355–358, https://doi.org/10.1016/j.scriptamat.2006.04.028.

[50] M. Reza-E-Rabby, K. Ross, N.R. Overman, M.J. Olszta, M. McDonnell, S.A. Whalen, Joining thick section aluminum to steel with suppressed FeAl intermetallic formation via friction stir dovetailing, Scr. Mater. 148 (2018) 63–67, https://doi.org/10.1016/j.scriptamat.2018.01.026.

[51] S. Kobayashi, T. Yakou, Control of intermetallic compound layers at interface between steel and aluminum by diffusion-treatment, Mater. Sci. Eng. A 338 (1–2) (2002) 44–53, https://doi.org/10.1016/S0921-5093(02)00053-9.

[52] D.I. Layner, A.K. Kurakin, Mechanism of the influence of silicon in aluminium on the reaction diffusion of iron, Fiz. Met. Metalloved. 18 (1) (1964) 145–148.

[53] A.K. Kurakin, Mechanism of the influence of silicon on the process of the reaction diffusion of iron in aluminium, Fiz. Met. Metalloved. 30 (1) (1970) 105–110.

[54] J.L. Song, S.B. Lin, C.L. Yang, C.L. Fan, Effects of Si additions on intermetallic compound layer of aluminum-steel TIG welding-brazing joint, J. Alloys Compd. 488 (1) (2009) 217–222, https://doi.org/10.1016/j.jallcom.2009.08.084.

[55] W.-J. Cheng, C.-J. Wang, Observation of hightemperature phase transformation in the Si-modified aluminide coating on mild steel using EBSD, Mater. Charact. 61 (4) (2010) 467–473, https://doi.org/10.1016/j.matchar.2010.02.001.

[56] D. Munson, A clarification of the phases occurring in aluminium-rich aluminium-iron-silicon alloys, with particular referanse to the ternary α-AlFeSi, J. Inst. Met. 95 (1967) 217–219.

[57] C.Y. Sun, L.F. Mondolfo, A clarification of the phases occurring in aluminium-rich aluminium-iron-silicon alloys, J. Inst. Met. 95 (1967) 384.

[58] H. Becker, T. Bergh, P.E. Vullum, A. Leineweber, Y. Li, Effect of Mn and cooling rates on α-, β- and δ-AlFeSi intermetallic phase formation in a secondary AlSi alloy, Materialia 5 (2019), https://doi.org/10.1016/j.mtla.2018.100198.

[59] A.L. Dons, Superstructures in α-Al(Mn,Fe,Cr)Si, Z. Met. 76 (2) (1985) 151–153.

[60] S.M. Arbo, T. Bergh, H. Solhaug, I. Westermann, B. Holmedal, Influence of thermomechanical processing sequence on properties of AA6082-IF steel cold roll bonded composite sheet, Procedia Manuf. 15 (2018) 152–160, https://doi.org/10.1016/j.promfg.2018.07.189.

[61] A.M.F. Muggerud, Y. Li, R. Holmestad, Composition and orientation relationships of constituent particles in 3xxx aluminum alloys, Philos. Mag. 94 (6) (2014) 556–568, https://doi.org/10.1080/14786435.2013.857796.

[62] B. Goldstein, J. Dresner, Growth of MgO films with high secondary electron emission on Al-Mg alloys, Surf. Sci. 71 (1) (1978) 15–26, https://doi.org/10.1016/0039-6028(78)90310-2.

[63] G.R. Wakefield, R.M. Sharp, The composition of oxides formed on Al-Mg alloys, Appl. Surf. Sci. 51 (1–2) (1991) 95–102, https://doi.org/10.1016/0169-4332(91)90065-R.

[64] C.R. Werrett, D.R. Pyke, A.K. Bhattacharya, XPS studies of oxide growth and segregation in aluminium-silicon alloys, Surf. Interface Anal. 25 (10) (1997) 809–816, https://doi.org/10.1002/(SICI)1096-9918(199709)25:10<809::AID-SIA304>3.0.CO;2-M.

[65] D.R. Cooper, J.M. Allwood, The influence of deformation conditions in solid-state aluminium welding processes on the resulting weld strength, J. Mater. Process. Technol. 214 (11) (2014) 2576–2592, https://doi.org/10.1016/j.jmatprotec.2014.04.018.

[66] H. Okamura, K. Aota, M. Sakamoto, M. Ezumi, K. Ikeuchi, Behaviour of oxides during friction stir welding of aluminium alloy and their effect on its mechanical properties, Weld. Int. 16 (4) (2002) 266–275, https://doi.org/10.1080/09507110209549530.

[67] Y.S. Sato, F. Yamashita, Y. Sugiura, S.H.C. Park, H. Kokawa, FIB-assisted TEM study of an oxide array in the root of a friction stir welded aluminium alloy, Scr. Mater. 50 (3) (2004) 365–369, https://doi.org/10.1016/j.scriptamat.2003.10.008.

[68] S. Kumari, S. Wenner, J.C. Walmsley, O. Lunder, K. Nisancioglu, Progress in understanding initiation of intergranular corrosion on AA6005 aluminum alloy with low copper content, J. Electrochem. Soc. 166 (11) (2019) C3114–C3123, https://doi.org/10.1149/2.0211911jes.

[69] K. Tanaka, M. Kumagai, H. Yoshida, Dissimilar joining of aluminum alloy and steel sheets by friction stir spot welding, J. Japan Inst. Light Metals 56 (6) (2006) 317–322.

[70] T. Ogura, Y. Saito, T. Nishida, H. Nishida, T. Yoshida, Partitioning evaluation of mechanical properties and the interfacial microstructure in a friction stir welded aluminum alloy/stainless steel lap joint, Scr. Mater. 66 (8) (2012) 531–534, https://doi.org/10.1016/j.scriptamat.2011.12.035.

[71] T. Ogura, T. Nishida, Y. Tanaka, H. Nishida, S. Yoshikawa, M. Fujimoto, A. Hirose, Microscale evaluation of mechanical properties of friction stir welded A6061 aluminium alloy/304 stainless steel dissimilar lap joint, Sci. Technol. Weld. Join. 18 (2) (2013) 108–113, https://doi.org/10.1179/1362171812Y.0000000098.

[72] V.I. Zheladnov, M.S. Makunin, P.M. Arzhanyi, Effect of oxygen in iron on the inhibition of diffusion in Al Fe bimetals, Metal Sci. Heat Treat. 18 (11) (1976) 978–981.

[73] G.M. Bedford, J. Boustead, The influence of oxygen and nitrogen on the growth of intermediate phases during the bonding of iron to aluminium, J. Mater. Sci. 13 (2) (1978) 253–260, https://doi.org/10.1007/BF00647768.

[74] T. Bergh, D.N. Johnstone, C.S. Allen, Scanning electron diffraction tilt series data of an aluminium-steel interface region [dataset], Zenodo (2020), https://doi.org/10.5281/zenodo.3938899.